Supporting Information

CoP/CoN Heterostructural Active Centers Supported on Nitrogen Carbon Nanorod Arrays as Freestanding High-performance Trifunctional Electrocatalysts

Linming Bai[a], Dan Wang[a], Hongchen Shen[b], Wenlong Wang[a], Shanshan Li[a]*, Wei Yan[a]*

a Xi'an Key Laboratory of Solid Waste Recycling and Resource Recovery, Department of Environmental Engineering, Xi'an Jiaotong University, Xi'an, 710049, China
b Department of Civil and Environmental Engineering, Rice University, Houston, TX, 77005, United States

* Corresponding author. E-mail address: yanwei@xjtu.edu.cn (W. Yan)
shanshan0320@xjtu.edu.cn (S.S.Li)

1. Characterization

The X-ray diffraction (XRD) was performed with Bruker D8 ADVANC. The scanning electron microscopy images were collected from Zeiss GeminiSEM 500 instrument. Transmission electron microscopy (TEM) analysis was carried out using a Thermofisher Talos F200X microscope. The valence distributions of elements in all samples were analyzed by a Thermofisher X-ray photoelectron spectroscopy (XPS, ESCALAB Xi+), operated at 16 kV, 14.9 mA. Samples were analyzed at a pass energy of 100 eV or 30 eV. The C1s peak with binding energy at 284.8 eV of adventitious carbon calibrated all peaks. The oxygen temperature-programmed desorption was tested on Autosorb-iQC-TPX (Quantachrome) and the specific measurements were listed in Table S1.

2. Electrochemical measurements

The ORR, OER and HER were measured with CHI 760e electrochemical workstation (CH Instruments Ins., USA) with a three-electrode system, in which the as-prepared samples worked as a working electrode, and graphitic rod and Hg/HgO were chosen as the counter electrode and reference electrode, respectively. All the test potentials were calibrated to the reversible hydrogen electrode (RHE) potential from *Eq*. (1):

$$E_{RHE} = E_{Hg/HgO} + 0.0591 \times pH + 0.098 \tag{1}$$

Linear sweep voltammetry (LSV) curves were tested with a scan rate of 5 mV s^{-1} and the geometric surface area of the working electrode was used for normalizing the obtained current density.

The Tafel slope (b) was calculated by *Eq*. (2):

$$\eta = a + b \times \log|j| \tag{2}$$

where η signifies the overpotential, a in this equation represents a constant.

The electrochemical active surface area (*ECSA*) was derived from *Eq*. (3):

$$ECSA = C_{dl} / C_s \tag{3}$$

where C_{dl} represents the electrochemical double-layer capacitance. Specifically, C_{dl} is the linear slope of Δj versus different scan rates, where $\Delta j = \left(\left(j_{anode} - j_{cathode} \right) / 2 \right)$ is the current at the middle potential of the potential window at varying scanning rates. In addition, the CV curves of OER in the range of 1.1 V and 1.2 V at 10-50 mV s^{-1} were investigated. Similarly, the CV curves of HER in the range of -0.7 V and -0.8 V were tested at scanning rates at 10-50 mV s^{-1}. *Cs* is specified with 0.040 mF cm^{-2}.

On the basis of LSV curves, the Koutechye-Levich (K-L) analysis (4-5) is applied to calculating the electron transfer number (n) in ORR process:

$$1/J = 1/J_K + 1/J_L = 1/J_K + 1/B\omega^{1/2} \tag{4}$$

$$B = 0.2nFC_0 \left(D_0 \right)^{2/3} \upsilon^{-1/6} \tag{5}$$

where J represents measured current density. J_K is kinetic current. J_L is diffusion limiting current density. ω is the rotation speed of the disk. F is Faraday's constant (C mol^{-1}). C_0 (mol cm^{-3})

and D_0 (cm^2 s^{-1}) are the bulk concentration of O$_2$ in 0.1 M KOH and the diffusion coefficient of O$_2$. υ (cm^2 s^{-1}) is the solution viscosity, which is specified as 0.01. Electrochemical impedance spectroscopy (EIS) was executed based on frequencies from 1 mHz to 10 kHz.

To further verify the n and HO_2^- yield of ORR, the rotating ring-disk electrode (RRDE) method was adopted according to the reported test method[9-10].

3. Metal-air battery measurements

Assembly of aqueous ZABs

A custom-made Zn-air cell was used to fabricate aqueous ZABs. The fabrication procedure started with the preparation of air cathodes. In the process, carbon paper and the nickel form are employed as gas diffusion layer and current collector, respectively. A flaky catalyst was fixed on the carbon paper, which was then attached to nickel foam. Using 6 mol L^{-1} KOH and 0.2 mol L^{-1} Zn(OAc)$_2$ solution as an electrolyte, the Zn plated and prepared air cathodes acted as anode and cathodes. The discharge polarization curve was obtained from CHI760e workstation. The galvanostatic discharge charge cycling measurements (battery life test) were executed with Microcurrent battery test systems (LAND CT3002A instrument, Wuhan LAND Electronic Co.Ltd., China).

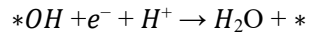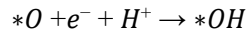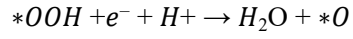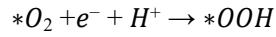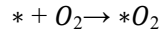Assembly of flexible all-solid-state Zinc-air battery

The electrolyte was prepared as follows: PVA (1 g) was dispersed in 24 mL deionized water, then heated and stirred for a period to obtain a clear solution. Then 1 mL mixture of 16 mol L^{-1} potassium hydroxide and 0.2 mol L^{-1} Zinc acetate dropwise and mixed at 95°C for a while. The resulting viscous solution was poured into the glass petri dish and frozen at -18°C for 12 h.

The prepared polymer electrolyte of PVA-KOH solution is sandwiched between a commercial Zn foil anode (1 cm × 3 cm) and air cathode (1 cm × 3 cm), fabricating to a flexible Zn-air battery. The Polyethylene terephthalate (PET) film with holes was used as an outer package to seal the device.

4. DFT calculation

The present first principle DFT calculations are performed by Vienna Ab initio Simulation Package (VASP 6.2.1)[1] with the projector augmented wave (PAW) method[2, 3]. The exchange-correlation energy was treated based on the generalized gradient approximation (GGA) by using Perdew-Burke-Ernzerhof (PBE) function[4]. The Monkhorst-Pack scheme with a k-point separate on length of 0.05 Å-1 was utilized for sampling the first Brillion zone[5], which was set as 3×3×1. The CoP (010) and CoN (010) surface models cut 3 and 4 layers from CoP and CoN bulk, respectively. The CoP-CoN model was combined by CoP (010) and CoN (010) surface for lattice matching, forming 5 layers heterojunction. The bottom layer of CoP and CoN models were fixed while the rest atoms were fully relaxed, and the whole atoms were fully relaxed in CoP-CoN model during all calculations. The self-consistent calculations apply a convergence energy threshold of 10^{-5} eV. The equilibrium lattice constants are optimized with maximum stress on each atom within 0.01 eV/Å.

The ORR is believed to process in the four electrons pathway[6.7],

$$* + O_2 \rightarrow *O_2$$

$$*O_2 + e^- + H^+ \rightarrow *OOH$$

$$*OOH + e^- + H+ \rightarrow H_2O + *O$$

$$*O + e^- + H^+ \rightarrow *OH$$

$$*OH + e^- + H^+ \rightarrow H_2O + *$$

Where, the * donates an active site on the catalyst.

To obtain the free energy profile, Gibbs free energies for all the states were calculated based on the ZPE-corrected DFT total energy, which was set as the enthalpy at 0 K. It can be calculated with:

$$G = H - TS = E_{DFT} + E_{ZPE} + \int_0^{298.15K} C_V dT - TS$$

where E_{DFT} is the total energy getting from DFT optimization, E_{ZPE} is the zero-point vibrational energy using the vibrational frequency calculations were performed via the finite-difference approach [8], C_V is the heat capacity, T is the kelvin temperature, and S is the entropy. The free energy for the gas-phase molecule was computed from thermodynamics by utilizing the standard thermodynamics data at the standard state.
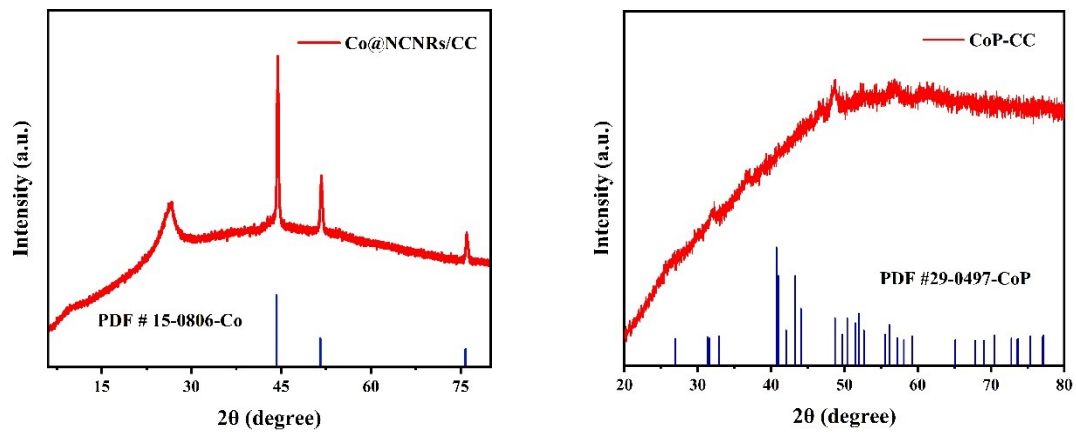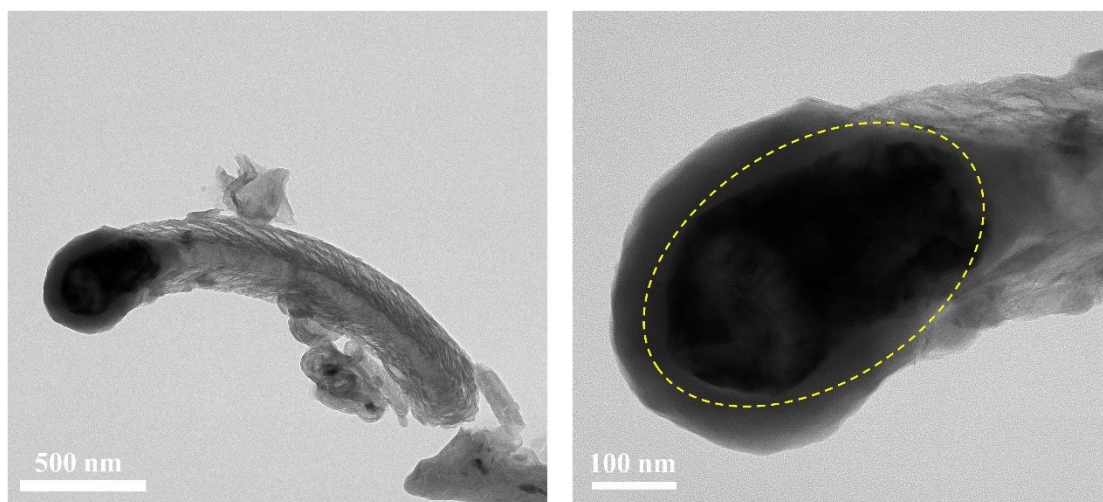
Fig. S1. XRD patterns of Co@NCNRs/CC and CoP/CC.

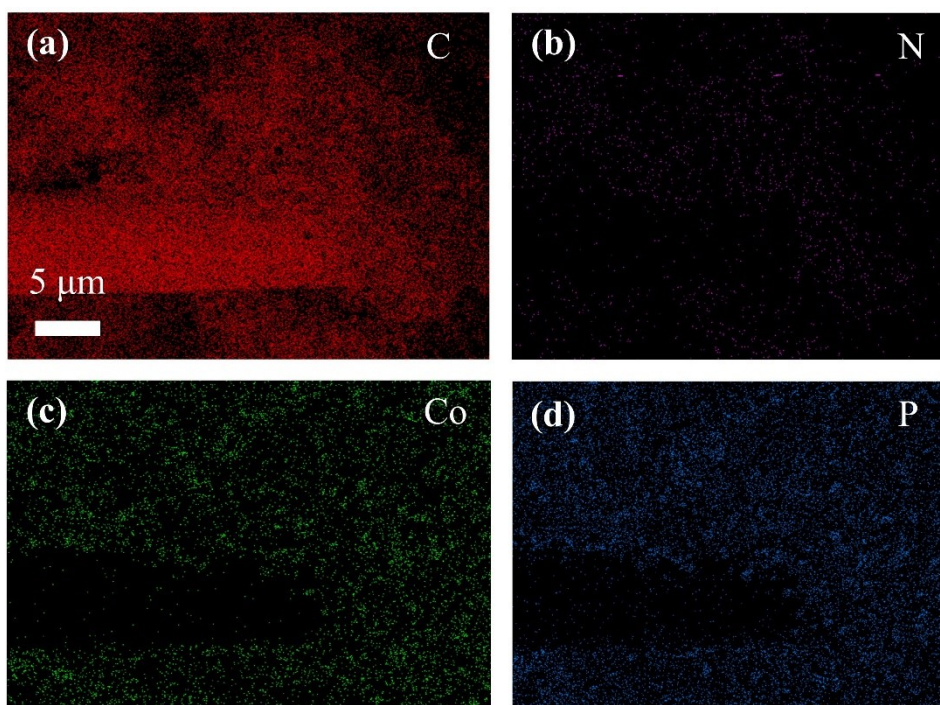Fig. S2. TEM images for the CoP/CoN particles are encapsulated in the carbon layer.

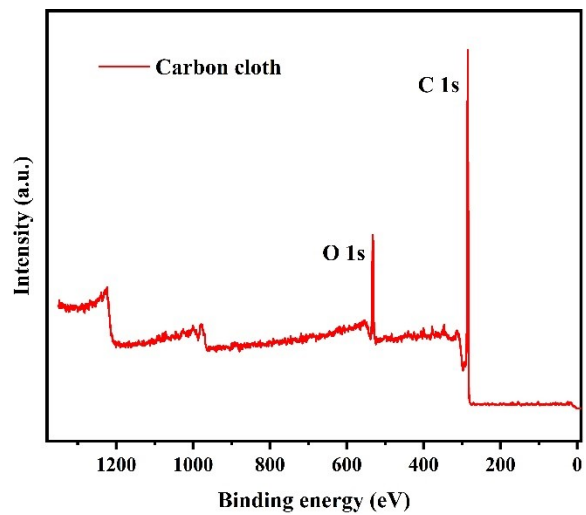Fig. S3. elemental mapping images of CoP/CoN@NCNRs/CC.

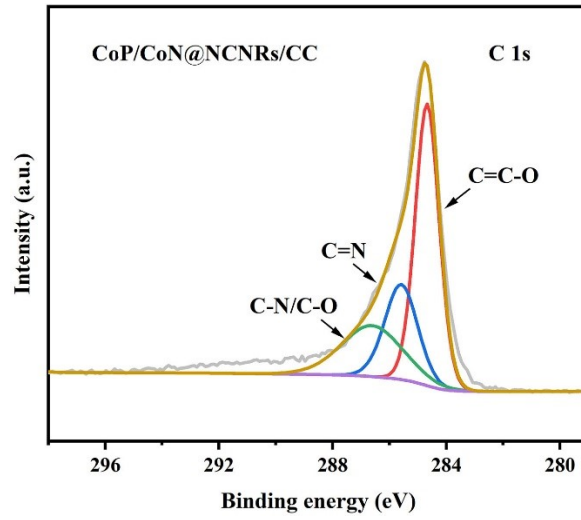Fig. S4. XPS survey spectrum of carbon cloth (CC).

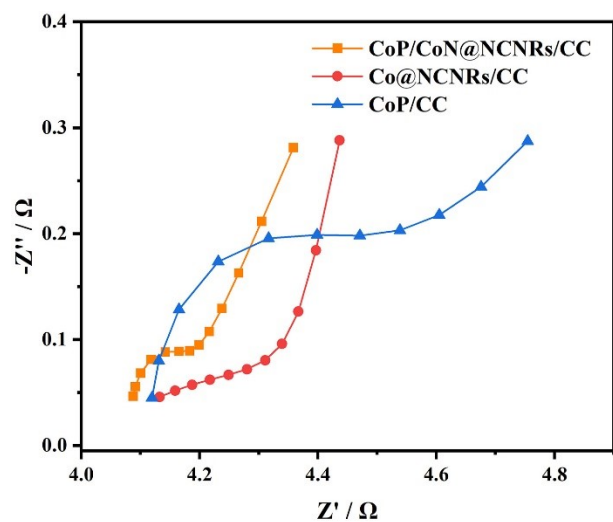Fig. S5. XPS survey spectrum C 1s of CoP/CoN@NCNRs/CC.

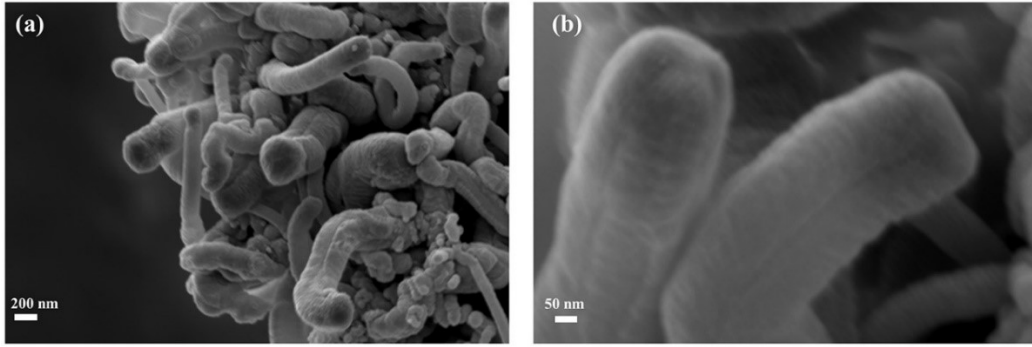Fig. S6. EIS plots for CoP/CoN@NCNRs/CC, Co@NCNRs/CC and CoP/CC.

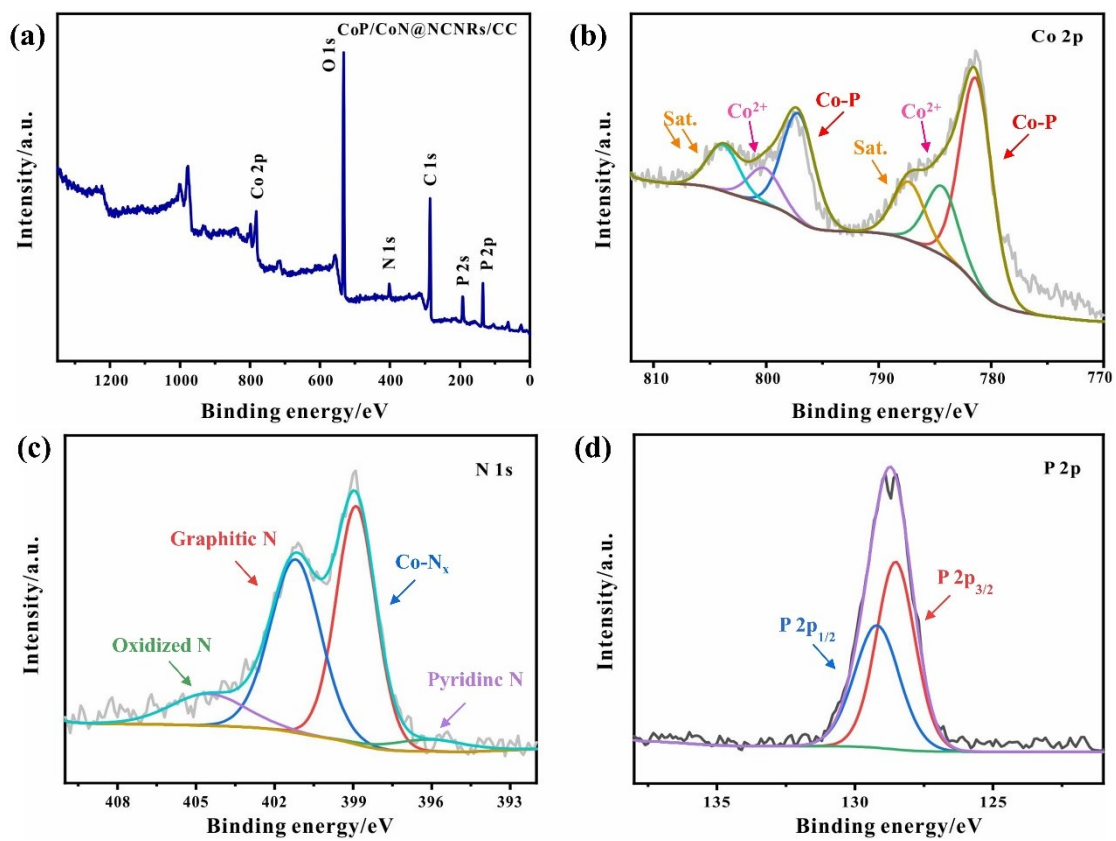Fig. S7. SEM of CoP/CoN@NCNRs/CC after cycle test.

Fig. S8. (a) XPS survey spectrum (b) Co 2p, (c) N 1s, and (d) P 2p of CoP/CoN@NCNRs/CC after cycle test.

Fig. S9. SEM of the acid sample.
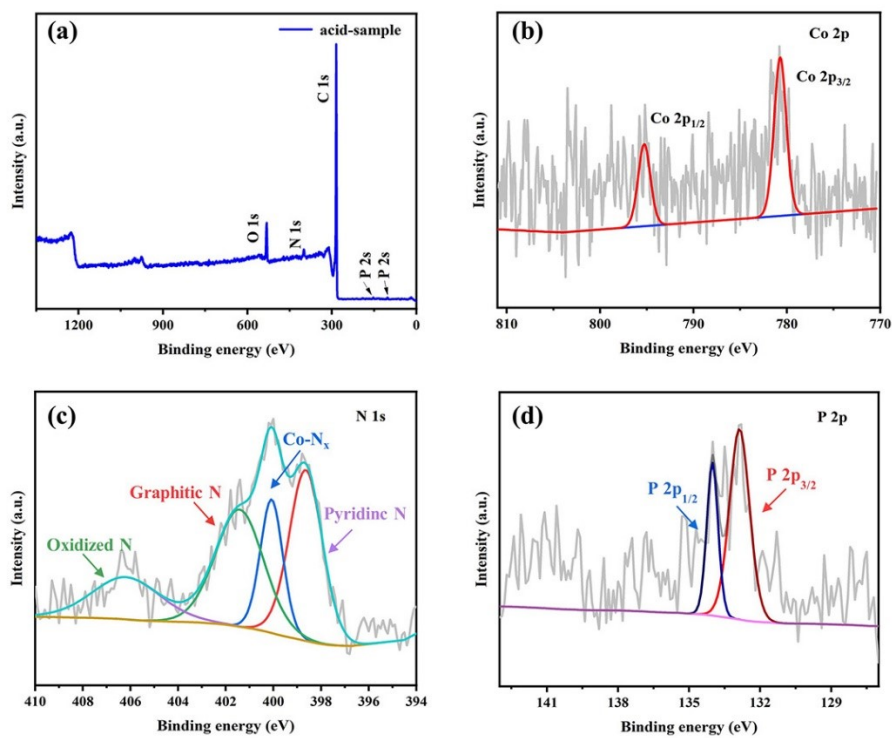
Fig. S10. (a) XPS survey spectrum (b) Co 2p, (c) N 1s, and (d) P 2p of the acid sample.
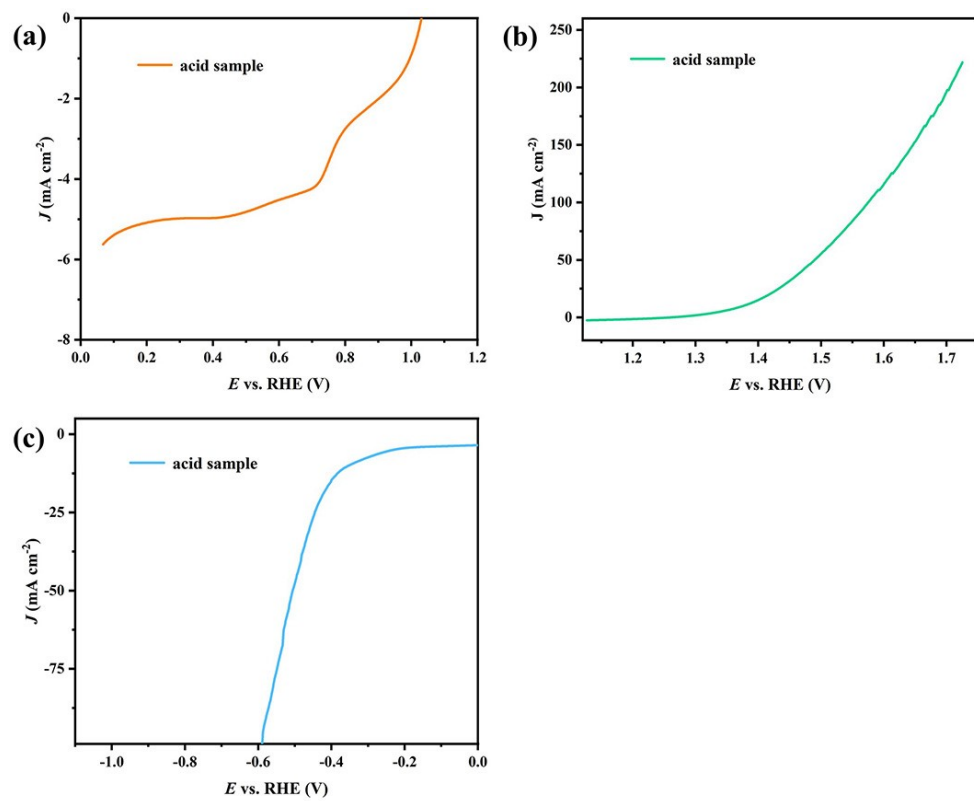
Fig. S11. (a) ORR curve; (b) OER curve and (c) HER curve of acid sample.
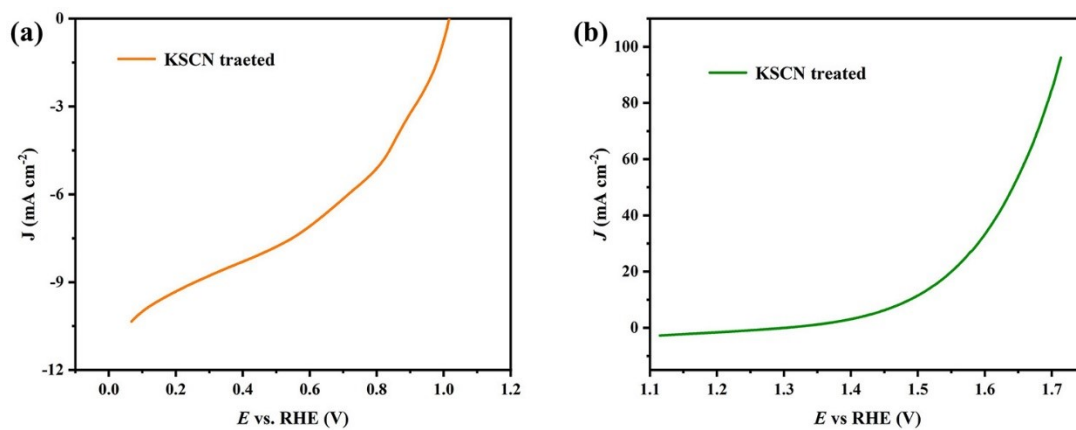
Fig. S12. ORR and OER curves of KSCN treated acid sample.
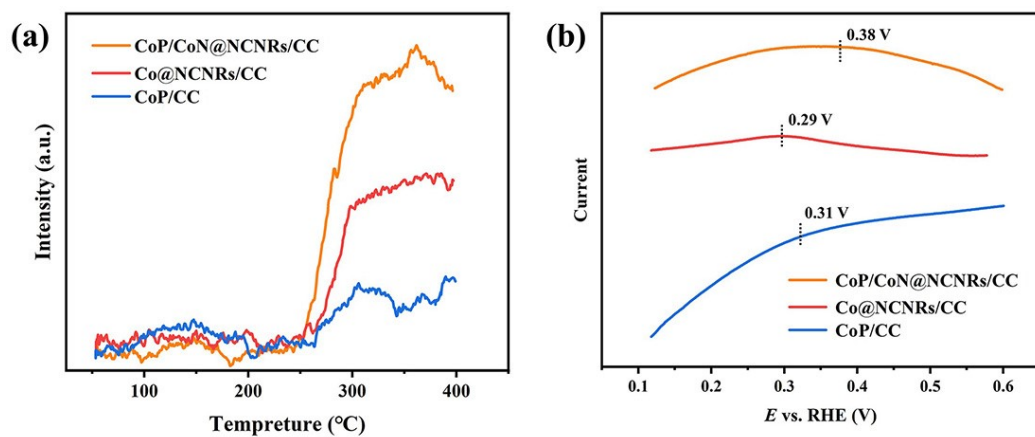
Fig. S13. (a) O$_2$-TPD curves of CoP/CoN@NCNRs/CC, Co@NCNRs/CC and CoP /CC. (b) Anodic scans showing the oxidative adsorption of hydroxide in N$_2$-saturated KOH solution for CoP/CoN@NCNRs/CC, Co@NCNRs/CC and CoP /CC. Currents here were normalized so that the curves could fit in the same plot.
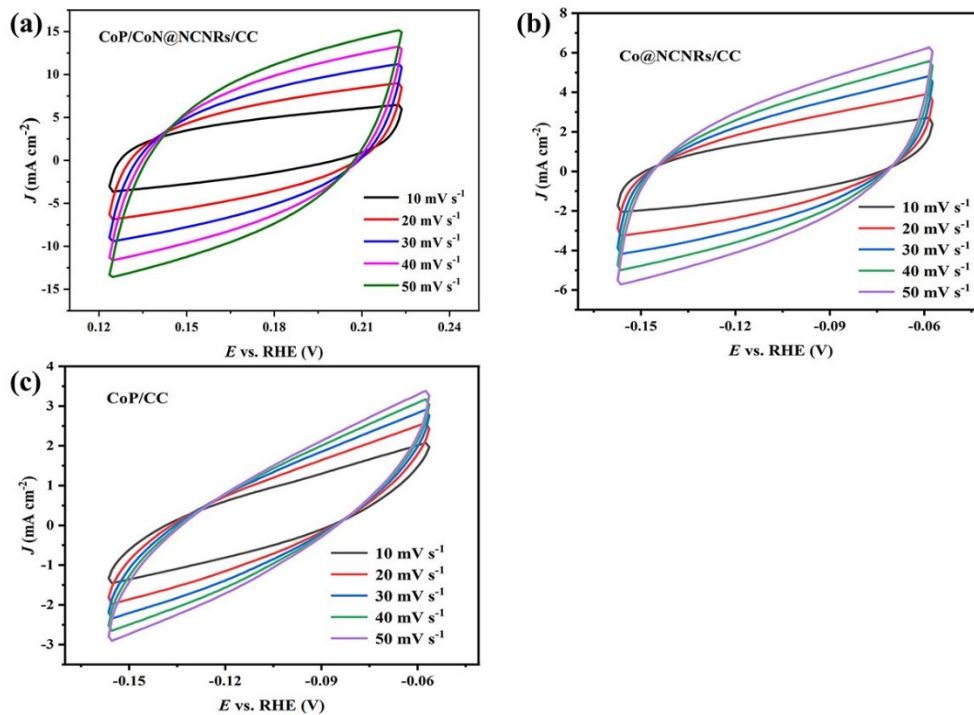
Fig. S14. CV curves under different scan rates for (a) CoP/CoN@NCNRs/CC; (b) Co@NCNRs/CC; (c) CoP/CC.
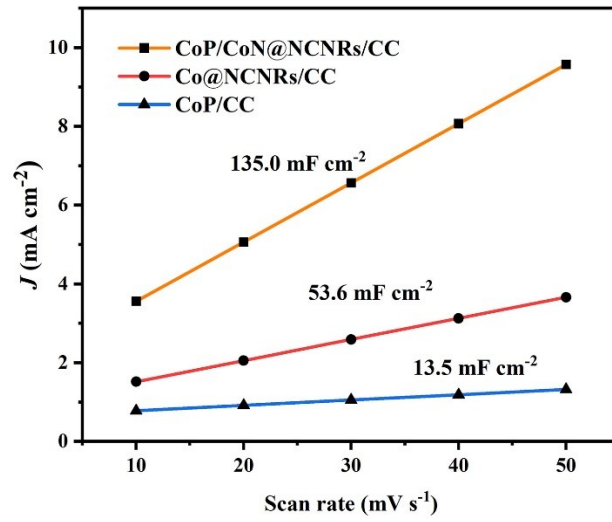
Fig. S15. Calculated C_{dl} for (a) CoP/CoN@NCNRs/CC; (b) Co@NCNRs/CC; (c) CoP/CC.
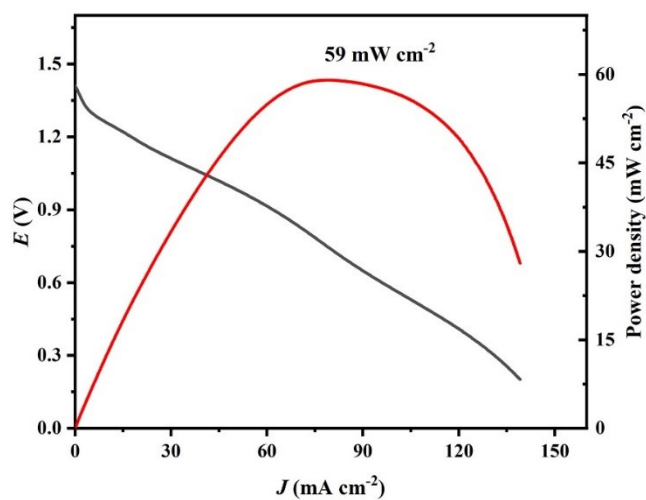
Fig. S16. Discharge curves and the power density curve for flexible ZAB.

Table S1.

Test procedures	Test details
Step 1	0.1 g of sample was purged with helium gas at 200°C for 2 h, and then cooled down to 50°C
Step 2	the sample was purged with 4% O_2/ He for 1 h
Step 3	the sample was slowly heated from ambient temperature to 400 °C at a heating rate of 10 ∘C min^{-1} in N_2 atmosphere

Table S2. Comparison of HER electrocatalytic activity of recently reported transition metal-based electrocatalysts in alkaline electrolyte.

Catalyst	$E_{j=10}$ / (V vs. RHE)	Tafel slope (mV dec^{-1})	Ref.
CoP/CoN@NCNRs/CC	165 mV	118	This work
CoFeN-NCNTs//CCM	151 mV	130	[9]
Co-N-MoO$_2$	258 mV	126.8	[10]
Co$_3$O$_4$/MoS$_2$	205 mV	128	[11]
CoP@PNC-DoS	173 mV	62.1	[12]
CoP/Ni$_2$P	200 mV	84	[13]
Co-NT/NF	178 mV	75	[14]
Co$_{0.85}$Se@NC	230 mV	125	[15]
CoTe	283 mV	90.5	[16]
Co/N-CNF	241 mV	132	[17]
CoLIm	162 mV	80.6	[18]
Zn-Co-S NN/CFP	234 mV	109	[19]
NiS−Ni(OH)$_2$@MoS$_{2+x}$/NF	226 mV	81	[20]
NCNT/CoFe-CoFe$_2$O$_4$	204	91	[21]

Table S3. Comparison of ZABs performance on recently reported transition metal-based electrocatalysts.

Catalyst	Peak power density (mW cm^{-2})	Specific Capacity (mAh g^{-1})	Cycling conditions	Ref.
CoP/CoN@NCNRs/CC	120	775	10 mA cm^{-2}, 30 min/cycle for 420 h	This work
CoNi@NCNTs/CC	138	782	5 mA cm^{-2}, 40 min/cycle for 370 h	[22]
NiFe@N-CFs	102	712	10 mA cm^{-2}, 40 min/cycle for 150 h	[23]
Fe$_{0.5}$Co$_{0.5}$O$_x$/NrGO	86	756	10 mA cm^{-2}, 2 h per cycle for 60 cycles	[24]
NiO/CoN PINWs	80	648	3 mA cm^{-2}, 10 min/cycle for 50 cycles	[25]
CoP@PNC-DoS	138.6	730.5	30 mA cm^{-2}, 30 min/cycle for 350 cycles	[12]
FeS/Fe$_3$C@N-S-C	63	N.A.	20 mA cm^{-2}, 10 min/cycle for 24 h	[26]
WN-Ni@N,P-CNT	126.2	827.8	5 mA cm^{-2}, 20 min/cycle for 330 h	[27]
CoS$_2$@MoS$_2$@NiS$_2$	80.8	~710	10 mA cm^{-2}, for 40 h	[28]

References

[1] G. Kresse and J. Furthmuller, Efficiency of ab-initio total energy calculations for metals and semiconductors using a plane-wave basis set, Computational Materials Science, 1996 (1) 15-50.

[2] P. E. Blochl, Projector augmented-wave method, Physical Review B, 1994 (24) 17953-17979.

[3] G. Kresse and D. Joubert, From ultrasoft pseudopotentials to the projector augmented-wave method, Physical Review B, 1999 (3) 1758-1775.

[4] J. P. Perdew, K. Burke, and M. Ernzerhof, Generalized gradient approximation made simple, Physical Review Letters, 1996 (18) 3865-3868.

[5] H. J. Monkhorst, and J. D. Pack, Special points for brillouin-zone integrations, Physical Review B, 1976 (12) 5188-5192.

[6] A. Kulkarni et al., Understanding Catalytic Activity Trends in the Oxygen Reduction Reaction, Chemical Reviews, 2018 (5) 2302-2312.

[7] Y. Nie, L. Li, and Z. D. Wei, Recent advancements in Pt and Pt-free catalysts for oxygen reduction reaction, Chemical Society Reviews, 2015 (8) 2168-2201.

[8] A. P. Scott and L. Radom, Harmonic vibrational frequencies: An evaluation of Hartree-Fock, Moller-Plesset, quadratic configuration interaction, density functional theory, and semiempirical scale factors, Journal of Physical Chemistry, 1996 (41) 16502-16513.

[9] G. Z. Zhou, G. S. Liu, X. B. Liu, Q. P. Yu, H. M. Mao, Z. Y. Xiao, et al., 1D/3D Heterogeneous Assembling Body as Trifunctional Electrocatalysts Enabling Zinc–Air Battery and Self-Powered Overall Water Splitting, Adv. Funct. Mater., 32 (2022) 2107608.

[10] L. J. Yang, J. Y. Yua, Z. Q. Wei, G. X. Li, L. D. Cao, W. J. Zhou, et al., Co-N-doped MoO_2 nanowires as efficient electrocatalysts for the oxygen reduction reaction and hydrogen evolution reaction, Nano Energy 41 (2017) 772–779.

[11] A. Muthurasua, V. Maruthapandianc, H. Y. Kim, Metal-organic framework derived Co_3O_4/MoS_2 heterostructure for efficient bifunctional electrocatalysts for oxygen evolution reaction and hydrogen evolution reaction, Applied Catalysis B: Environmental 248 (2019) 202–210.

[12] Y. P. Li, Y. Liu, Q. Z. Qian, G. R. Wang, G. Q. Zhang, Supramolecular assisted one-pot synthesis of donut-shaped CoP@PNC hybrid nanostructures as multifunctional electrocatalysts for rechargeable Zn-air batteries and self-powered hydrogen production, Energy Storage Materials 28 (2020) 27–36.

[13] L. L. Chai, Z. Y. Hu, X. Wang, Y. W. Xu, L. J. Zhang, T. T. Li, Stringing Bimetallic Metal–Organic Framework-Derived Cobalt Phosphide Composite for High-Efficiency Overall Water Splitting, Adv. Sci. 7 (2020) 1903195.

[14] J. Zhang, M. Song, J. Wang, Z. X. Wu, X. E. Liu, In-situ transformation to accordion-like core-shell structured metal@metallic hydroxide nanosheet from nanorod morphology for overall water-splitting in alkaline media, Journal of Colloid and Interface Science 559 (2020) 105-114.

[15] T. Meng, J. W. Qin, S. G. Wang, D. Zhao, B. G. Mao, M. H. Cao, In situ coupling of $Co_{0.85}Se$ and N-doped carbon via one-step selenization of metal–organic frameworks as a trifunctional catalyst for overall water splitting and Zn–air batteries, J. Mater. Chem. A, 5 (2017) 7001-7014.

[16] M. Nath, U. D. Silva, H. Singh, M. Perkins, W. P. R. Liyanage, S. Umapathi, Cobalt Telluride: A Highly Efficient Trifunctional Electrocatalyst for Water Splitting and Oxygen Reduction, ACS Appl. Energy Mater. 4 (2021) 8158-8174.

[17] J. Liu, J. S. Zhou, M. K. H. Leung, Valence Engineering of Polyvalent Cobalt Encapsulated in a Carbon Nanofiber as an Efficient Trifunctional Electrocatalyst for the Zn−Air Battery and Overall

Water Splitting, ACS Appl. Mater. Interfaces, 14 (2022) 4399-4408.

[18] E. Armakola, M. Gjika, A. Visa, M. B. García, P. O. Pastor, D. C. Lazarte, et al., Exploiting the Multifunctionality of M^{2+}/Imidazole−Etidronates for Proton Conductivity (Zn^{2+}) and Electrocatalysis (Co^{2+}, Ni^{2+}) toward the HER, OER, and ORR, ACS Appl. Mater. Interfaces 14 (2022) 11273-11287.

[19] X. Y. Wu, X. P. Han, X. Y. Ma, W. Zhang, Y. D. Deng, C. Zhong, et al., Morphology-Controllable Synthesis of Zn−Co-Mixed Sulfide Nanostructures on Carbon Fiber Paper Toward Efficient Rechargeable Zinc−Air Batteries and Water Electrolysis, ACS Appl. Mater. Interfaces 9 (2017) 12574-12583.

[20] J. M. Bai, T. Meng, D. L. Guo, S. G. Wang, B. G. Mao, M. H. Cao, Co_9S_8@MoS_2 Core−Shell Heterostructures as Trifunctional Electrocatalysts for Overall Water Splitting and Zn−Air Batteries, ACS Appl. Mater. Interfaces 10 (2018) 1678-1689.

[21] Q. Qin, P. Li, L. L. Chen, X. E. Liu, Coupling Bimetallic Oxides/Alloys and N-Doped Carbon Nanotubes as Tri-Functional Catalysts for Overall Water Splitting and Zinc−Air Batteries, ACS Appl. Mater. Interfaces 10 (2018) 39828-39838.

[22] W. W. Tian, J. T. Ren, Z. Y. Yuan, In-situ cobalt-nickel alloy catalyzed nitrogen-doped carbon nanotube arrays as superior freestanding air electrodes for flexible zinc-air and aluminum-air batteries, Applied Catalysis B: Environmental 317 (2022) 121764.

[23] Y. Niu, X. Teng, S. Gong, Z. Chen, A bimetallic alloy anchored on biomass-derived porous N-doped carbon fibers as a self-supporting bifunctional oxygen electrocatalyst for flexible Zn–air batteries, J. Mater. Chem. A, 8 (2020) 13725-13734.

[24] L. Wei, H. E. Karahan, S. Zhai, H. Liu, X. Chen, Z. Zhou, et al., Amorphous Bimetallic Oxide-Graphene Hybrids as Bifunctional Oxygen Electrocatalysts for Rechargeable Zn-Air Batteries, Adv. Mater., 29 (2017) 1701410.

[25] J. Yin, Y. Li, F. Lv, Q. Fan, Y.Q. Zhao, Q. Zhang, et al., NiO/CoN Porous Nanowires as Efficient Bifunctional Catalysts for Zn-Air Batteries, ACS Nano, 11 (2017) 2275-2283.

[26] F. T. Kong, X. H. Fan, A. G. Kong, Z. Q. Zhou, X. Y. Zhang, Y. K. Shan, Covalent Phenanthroline Framework Derived FeS@Fe_3C Composite Nanoparticles Embedding in N-S-Codoped Carbons as Highly Efficient Trifunctional Electrocatalysts, Adv. Funct. Mater., 28 (2018) 1803973.

[27] Q. Zhang, F. Luo, X. Long, X. X. Yu, K. G. Qu, Z. H. Yang, N, P doped carbon nanotubes confined WN-Ni Mott-Schottky heterogeneous electrocatalyst for water splitting and rechargeable zinc-air batteries, Applied Catalysis B: Environmental 298 (2021) 120511.

[28] X. Li, Z. H. Yin, M. Cui, L. Gao, A. M. Liu, W. N. Su, et al., Double shelled hollow CoS_2@MoS_2@NiS_2 polyhedron as advanced trifunctional electrocatalyst for zinc-air battery and self-powered overall water splitting, Journal of Colloid and Interface Science 610 (2022) 653-662.